Nanoscale

ROYAL SOCIETY OF CHEMISTRY

PAPER

View Article Online
View Journal | View Issue

Cite this: *Nanoscale*, 2023, **15**, 17609

Periodic arrays of structurally complex oxide nanoshells and their use as substrate-confined nanoreactors†

Walker J. Tuff,[a] Robert A. Hughes,[a] Brendan D. Nieukirk,[b] Luca Ciambriello,[a,c] Robert D. Neal,[a] Spencer D. Golze,[a] Luca Gavioli[c] and Svetlana Neretina *[a,b]

Received 29th August 2023,
Accepted 18th October 2023

DOI: 10.1039/d3nr04345b

rsc.li/nanoscale

Sacrificial templates present an effective pathway for gaining high-level control over nanoscale reaction products. Atomic layer deposition (ALD) is ideally suited for such approaches due to its ability to replicate the surface topography of a template material through the deposition of an ultrathin conformal layer. Herein, metal nanostructures are demonstrated as sacrificial templates for the formation of architecturally complex and deterministically positioned oxide nanoshells, open-topped nanobowls, vertically standing half-shells, and nanorings. The three-step process sees metal nanocrystals formed in periodic arrays, coated with an ALD-deposited oxide, and hollowed out with a selective etch through nanopores formed in the oxide shell. The procedure is further augmented through the use of a directional ion beam that is used to sculpt the oxide shells into bowl- and ring-like configurations. The functionality of the so-formed materials is demonstrated through their use as substrate-confined nanoreactors able to promote the growth and confinement of nanomaterials. Taken together, the work expands the design space for substrate-based nanomaterials, creates a platform for advancing functional surfaces and devices and, from a broader perspective, advances the use of ALD in forming complex nanomaterials.

Introduction

Atomic layer deposition (ALD) has emerged as a transformative thin film deposition technique with enabling capabilities that have become indispensable to the semiconductor industry.[1–5] Its rise to prominence has been contingent upon an unrivaled set of competencies, foremost of which is the ability to deposit uniformly thick, pinhole-free conformal layers over three-dimensional topographies, including those with high aspect ratios and nanoscale features. Further significance is derived from nanometer-scale thickness control, low to moderate processing temperatures, compositional uniformity, an ever-expanding library of materials that are accessible to the technique, and the ability to deposit multilayers with sharp interfaces. These desirable characteristics are complemented by the emergence of highly automated deposition systems offering fine and reproducible controllability, ease-of-use, and wafer-scale deposition areas. As with any technique, ALD has its drawbacks, including low deposition rates, a limited choice of accessible materials, processing windows that are often unable to promote a high degree of crystallinity, and a high acquisition cost. The overall deposition strategy is one that sequentially exposes a heated substrate surface to two vapor-phase precursor chemicals in a nonoverlapping manner where each is responsible for a self-limiting half-reaction that proceeds until the substrate surface is saturated with up to one monolayer. Deposition, hence, occurs in a layer-by-layer manner by cycling the two precursors until the desired film thickness is obtained. This strategy not only stands out as unique among deposition techniques but endows ALD with capabilities for which there is no suitable alternative.

Given the unique status of ALD, it is not surprising that it is now being successfully integrated into numerous nanofabrication processes and nanomaterial synthesis schemes.[6–11] When protected by ALD-deposited oxide layers, environmentally sensitive nanomaterials can attain air-stability,[12–15] become resistant to leaching in aqueous media,[12,16–18] and withstand extreme pH and other chemically aggressive environments.[16,19,20] The chemical barrier provided allows for the preservation of plasmonic properties in readily oxidized

[a]*College of Engineering, University of Notre Dame, Notre Dame, Indiana 46556, Unites States. E-mail: sneretina@nd.edu*
[b]*Department of Chemistry and Biochemistry, University of Notre Dame, Notre Dame, Indiana 46556, USA*
[c]*Interdisciplinary Laboratories for Advanced Materials Physics (i-LAMP), Dipartimento di Matematica e Fisica, Università Cattolica del Sacro Cuore, 25133 Brescia, Italy*

† Electronic supplementary information (ESI) available. See DOI: https://doi.org/10.1039/d3nr04345b

metals such as Cu and Ag and has forwarded a chemical sensing modality referred to as shell-isolated nanoparticle-enhanced Raman spectroscopy (SHINERS).[21,22] The chemical inactivity of these same oxide layers can also be exploited as a means to passivate surfaces against unwanted dendritic growth on the anodes of lithium metal batteries[20] or whisker formation on electronic assemblies.[23] With metal nanostructures being highly susceptible to morphological transformations at elevated temperatures, ALD-deposited oxides have also proven effective in impeding the surface diffusion pathways responsible for these changes. In this role, they have preserved the shape-dependent properties of nanometals,[12,24,25] inhibited nanoparticle sintering,[17,18,26–29] and allowed for improvements to nanostructure crystallinity.[30] This has allowed for the use of these materials in high-temperature applications related to catalysis[11] and refractory plasmonics.[31] The nanometal–oxide combination is not merely restricted to functionalities related to nanometal stabilization. ALD-deposited TiO_2 has, for example, been used to forward cooperative metal–semiconductor phenomena of relevance to photocatalysis,[32] photovoltaics,[6,33,34] and the performance and monitoring of self-cleaning surfaces.[16,35] Similarly, plasmon-enhanced fluorescence applications have benefitted from ultrathin oxide coatings that allow plasmonic near-fields to penetrate while simultaneously acting as a dielectric spacer that prevents the quenching of an adjacent fluorescent material by the nanometal.[21] Collectively, these examples demonstrate the utility of ALD-deposited oxides in fabricating functional nanomaterials.

Apart from a nanostructure coating technology, there exists an emergent set of synthesis techniques that realize nanomaterials by using either the ALD-deposited layer or an adjacent material as a sacrificial entity. The preparation of (i) free-standing ALD layers through the dissolution of a sacrificial substrate,[8] (ii) the high-temperature desorption of Cu from Al_2O_3-coated Cu nanowires,[36] (iii) the coating of electrospun fibers,[7] carbon nanocoils,[37] polymeric structures,[38,39] or cellulose[40] followed by the removal of the core material through calcination, and (iv) the application of a conformal etch-resistant layer to a nanostructured template (*e.g.*, anodic aluminum oxide, metal organic frameworks) followed by the removal of the template in a liquid etchant,[10] all provide conceptually straightforward examples of this strategy. The formation of sub-10 nm air-filled plasmonic nanogaps with tunable widths have relied upon the use of a sacrificial ALD-deposited oxide that first defines a dielectric-filled nanogap between adjacent metal structures, after which it is removed with a selective etch.[41–44] Sacrificial oxide layers formed over substrate-bound Au nanostructures, followed by their partial removal, have also proven effective in directing liquid-state nanometal syntheses toward the formation of periodic arrays of aligned bimetallic Janus nanocrystals.[45] Collectively, these various schemes demonstrate ALD-enabled synthesis techniques as a viable means for generating otherwise unobtainable nanomaterials and provides the impetus for pursuing related strategies.

The liquid-phase synthesis of metal nanocrystals directly on substrate surfaces is a rapidly expanding field that is increasingly realizing greater levels of shape-control and the ability to deterministically position nanoscale objects at site-specific locations.[46–48] Similar capabilities, however, have not been demonstrated for oxide materials. Herein, a nanofabrication strategy is forwarded that utilizes metal nanocrystals as sacrificial templates that, when used in combination with ALD and Ar^+ ion milling, form periodic arrays of oxide nanoshells, open-topped bowls, vertically standing half-shells, and shape-controlled rings. The structures are demonstrated as substrate-confined nanoreactors able to support the synthesis of nanomaterials within their confines. The work contributes to an overall effort that is advancing wafer-based syntheses beyond traditional top-down lithographic approaches by creating alternative platforms with first-of-their-kind capabilities.

Results

Fig. 1a shows a schematic of the devised procedure for forming periodic arrays of air-filled HfO_2 nanoshells. An array of single-crystal Au nanoparticles (NPs) is first formed using nanoimprint lithography in combination with a high-temperature templated assembly process, the details of which are described elsewhere.[49] ALD is then used to deposit a 5 nm thick conformal HfO_2 layer over the arrayed structures as well as the exposed substrate surface. With Au@HfO_2 core–shell structures formed, the desired product can be achieved if the Au is etched away through pinholes in the HfO_2 layer. For this purpose, *aqua regia* is a suitable chemical etchant since it readily etches Au while leaving HfO_2 intact. There are, however, no pinholes in the as-deposited 5 nm thick HfO_2 layer. As such, they were induced with a heating regimen that sees nanopore(s) formed at each of the array sites. Pore formation at elevated temperatures has been previously observed in ALD-deposited oxide layers[50,51] and is a direct consequence of the fact that such layers are typically deposited as amorphous materials that, when heated, densify. It is this reorganization at the atomic level that gives rise to a low-level porosity that provides the access points from which the Au is etched. It should be noted that the overall strategy is not restricted to the Au–HfO_2 combination since a suitable selective etch can be found for nearly every elemental metal.

The heat treatment used to form nanopores and the subsequent Au etching process were monitored and optimized using spectroscopy and SEM imagery. For all experiments, a 5 nm thick layer of HfO_2 was used since thinner layers lack mechanical rigidity and, as a result, collapse due to the capillary forces exerted when the nanoshells are removed from the etchant, rinsed, and then dried (see ESI, Fig. S1†). It was determined that an anneal temperature of 770 °C is required to induce pinholes in a timely fashion. Fig. 1b shows the extinction spectra obtained as a single sample progressed through the procedure shown in Fig. 1a. The uncoated Au NPs exhibit a prominent plasmon at 624 nm that red-shifts to 659 nm and

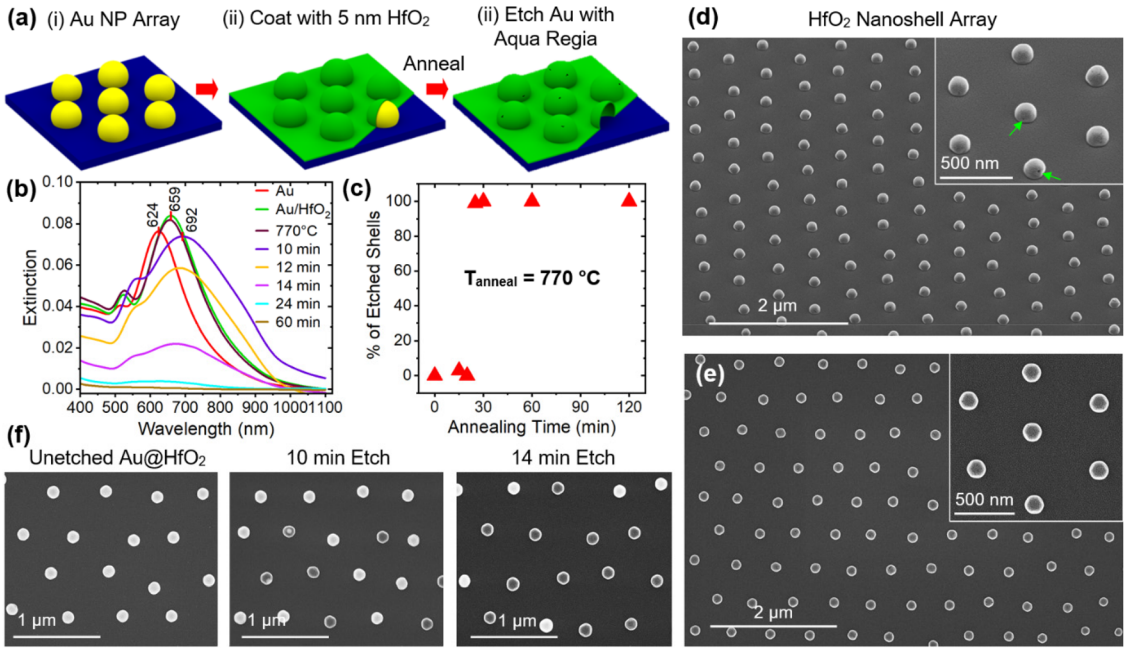

Fig. 1 (a) Schematic depicting the three-stage procedure for forming periodic arrays of air-filled HfO_2 nanoshells. Note that the bottom right corner of the second- and third-stage schematics show HfO_2 cutaways revealing the internal structure of the nanoshells. (b) Extinction spectra obtained as the Au NP array is coated with HfO_2, annealed at 770 °C for 30 min, and then exposed to an *aqua regia* etch for various time intervals. (c) Plot showing the percentage of successfully etched nanoshells as a function of anneal time. (d) Tilted- and (e) top-view SEM images of a HfO_2 nanoshell array formed under optimum conditions. (f) Top-view SEM images showing the Au etching process at various stages where bright and dark NPs correspond to unetched and fully etched nanoshells, respectively. Note that the array shown in (e) provides an image of the fully etched structures.

intensifies once a 5 nm conformal HfO_2 layer is deposited on its surface, a result that is anticipated when a dielectric coating is applied to a plasmonic NP.[52] The 770 °C heat treatment has little influence on the plasmon. The nanopores formed, however, facilitate the Au etching process that occurs over a 60 min interval and appears as a plasmon that steadily diminishes to the point of extinction. The substantial red shift to 692 nm for these spectra originates from the fact that the etching process was monitored *in situ*, and as such, the nanostructures were immersed in a liquid etchant with an index of refraction near that of H_2O.

SEM characterization of the nanoshells allows for a statistical assessment of the success rate of shell formation under various conditions since hollowed structures are easily distinguished from those filled or partially filled with Au. Fig. 1c is a plot showing the percentage of fully etched nanoshells as a function of anneal time for a constant etch time of 60 min. It reveals a rather abrupt rise in the success rate from near zero to close to 100% occurring after 20 min. This sharp rise, which indicates that almost all structures are behaving identically, is likely attributable to the uniformity of the amorphous HfO_2 layer as well as the consistent size and shape expressed by the Au NPs. Although this data seems to indicate that anneal times as long as 120 min are acceptable, these long intervals are considered less than optimal since they allow for a continuation of the HfO_2 densification process whereby nanopores often evolve into sizable cracks (see ESI, Fig. S2†). On the basis of these findings, a 30 min anneal time is considered optimal but where it should be recognized that this time is dependent on a number of factors including the (i) HfO_2 layer thickness, (ii) ALD deposition conditions, and (iii) size, geometry, and composition of the metal NPs. Fig. 1d and e shows SEM images of the HfO_2 nanoshell array formed under optimum conditions that were taken at a 55° tilt angle and at normal incidence. The shells, which appear near-hemispherical, have a diameter of 160 nm and are devoid of Au. They rarely exhibit nanopores that are resolvable in SEM but two are clearly visible in the inset of Fig. 1d (denoted by green arrows). Fig. 1f presents an etching time progression that shows Au@HfO_2 core–shell structures that are unetched followed by those where the etching process was halted at 10 and 14 min. The data taken at intermediate etching times is somewhat unexpected in that it shows that many of the Au NPs remain intact while others have been completely removed. This could indicate that, for many of the structures, the nanopores are not completely formed after the annealing step but instead only exist as weak points that are breached after they are placed in Au etchant. In such a scenario, etching of the Au structure would initially be inhibited but once begun would occur at a fairly rapid rate. This explanation is consistent with our *in situ* spectroscopic monitoring of the etching process that shows a 10 min delay before any appreciable etching occurs (see ESI, Fig. S3†). It should, however, be understood that the annealing process is essential to nanopore formation since unannealed

samples are highly impermeable and are even robust to an overnight exposure to *aqua regia* (see ESI, Fig. S4†). Taken together, these results validate the nanoshell fabrication strategy and show that high-temperature anneals provide an effective means to form nanopores in ALD-deposited HfO_2.

A key feature of the nanoshell fabrication strategy is its ability to replicate the surface topography of the template material. As such, nanoshell shape-control is entirely dependent upon defining templates with the desired shape. The seed-mediated colloidal synthesis of metal nanostructures has demonstrated mastery over shape-control where there now exists a vast collection of protocols capable of defining nanostructures with well-defined geometries at high yield. Many of these same syntheses can be carried out on substrate-based seeds to realize periodic arrays of architecturally complex nanostructures[46–48] which can, in turn, be transformed into nanoshells with the same shape. Fig. 2a shows a schematic of the overall strategy. It begins by forming an array of single-crystal Au NPs in the same manner as previously described. These structures are then transformed into Au@Ag core–shell nanostructures by placing them in a 95 °C aqueous solution of $AgNO_3$ and trisodium citrate (Na_3CA).[53] The ensuing reaction sees Ag deposited onto the Au surface and the emergence of (100) faceting. With the resulting structures expressing a cube-like morphology, they are then transformed into HfO_2 nanoshells of identical shape using the same coating–annealing–etching methodology. By merely changing the solution-based synthesis (*i.e.*, step ii), the shape of the nanoshell can be varied.[54,55] Fig. 2b–d shows SEM images of nanocube, nanostar, and nanoplate templates (top row) and the resulting HfO_2 nanoshells taken from top and side view perspectives (middle and bottom row). For all cases, the shell material accurately

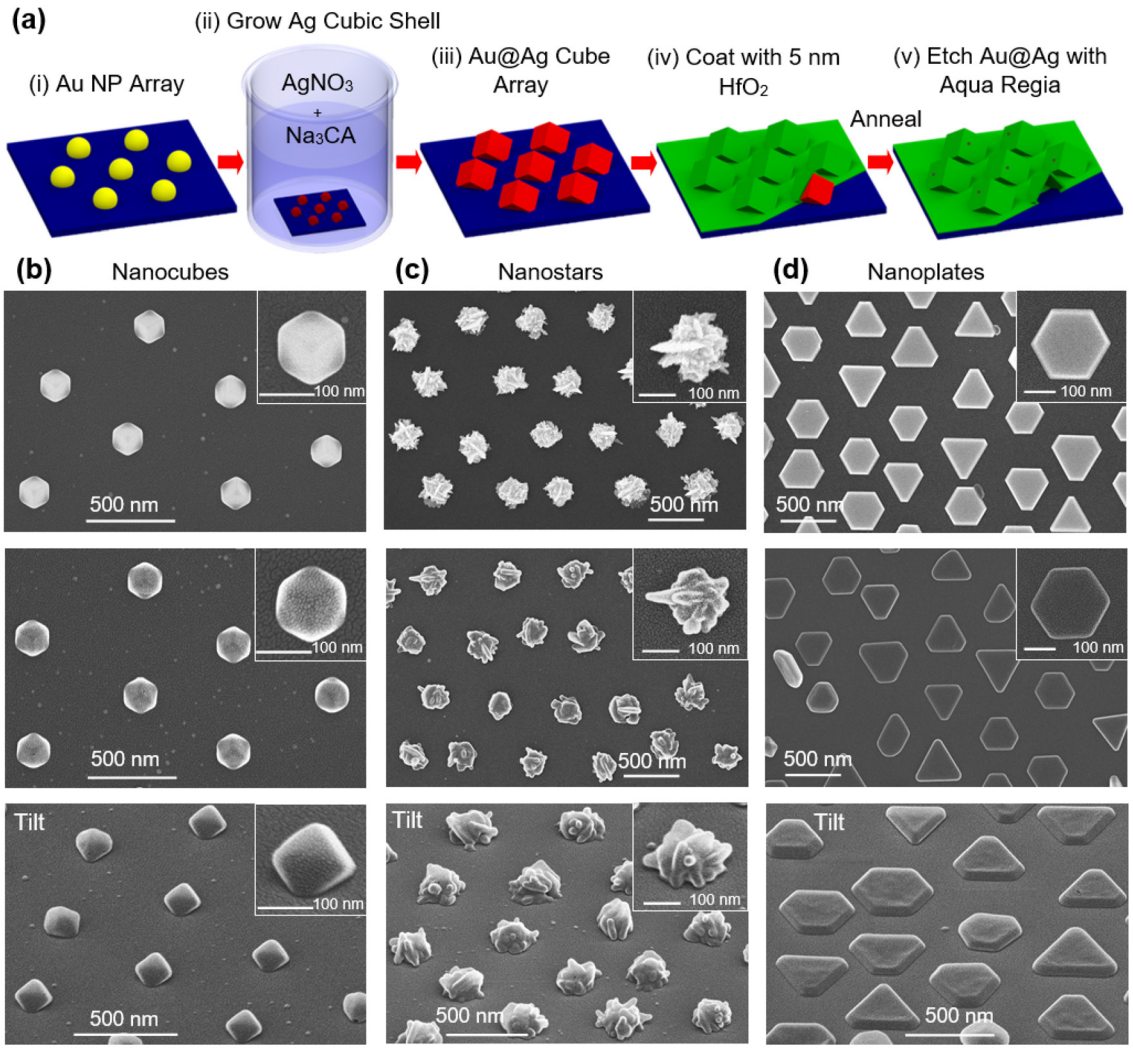

Fig. 2 (a) Schematic of the nanofabrication process used to form hollow HfO_2 shells with complex architectures. SEM images of the (b) Au@Ag core–shell nanocubes, (c) Au nanostars and (d) Au nanoplates (top row) that are used as sacrificial templates and the HfO_2 nanoshells derived from them (middle and bottom row).

replicates the surface topology of the template where the intricacy of the nanostar shells underscores ALD's ability to replicate complex topographies.

With nanopores providing channels through which liquids can enter or leave the HfO_2 nanoshell, such structures can be utilized as substrate-confined nanoreactors.[56] In demonstration of this capability, a series of experiments were carried out in which noble metal nanostructures were synthesized within the confines of HfO_2 shells. HfO_2 is well-suited for such applications due to its ability to withstand high temperatures and chemically aggressive environments.[12,16] Fig. 3a shows a schematic of the procedure used to form an array of nanoporous Au structures[57] where each structure is confined within a 5 nm thick HfO_2 shell. It begins with the fabrication of polycrystalline Au–Ag–Au trilayer disks followed by a high-temperature solid-state dewetting process that causes each disk to assemble into a well-alloyed AuAg nanostructure with a near-hemispherical geometry. Then, using the aforementioned procedures, structures are coated with a conformal HfO_2 layer and heated to induce nanopore formation. When exposed to a HNO_3 etch, the AuAg structures undergo a dealloying process that selectively removes Ag as the remaining Au assumes a porous configuration. Fig. 3b and c shows backscattered electron (BSE) SEM images of structures formed where the porosity of the Au is clearly visible. It is noteworthy that these structures express a similar morphology with those produced in the absence of a nanoshell (see ESI, Fig. S5†). Spherical Au and Ag NPs were also formed within the confines of the nanoshell by sequentially immersing hollow shells in ascorbic acid (AA) and aqueous $HAuCl_4$ (or $AgNO_3$) where repeated cycles led to the formation of additional particles (Fig. 3d). Elemental mapping derived from energy-dispersive spectroscopy (EDS) measurements confirm the presence of Au and Ag within the shells (Fig. 3e). Other demonstrations saw these Au NPs seed Au nanowires (Fig. 3f) or nanoplates (Fig. 3g). Even though such syntheses have not yet been optimized, they nevertheless demonstrate the potential of HfO_2 shells to promote the growth and confinement of nanomaterials.

Through the integration of directional Ar^+ ion milling into nanofabrication process, it was possible to further expand the

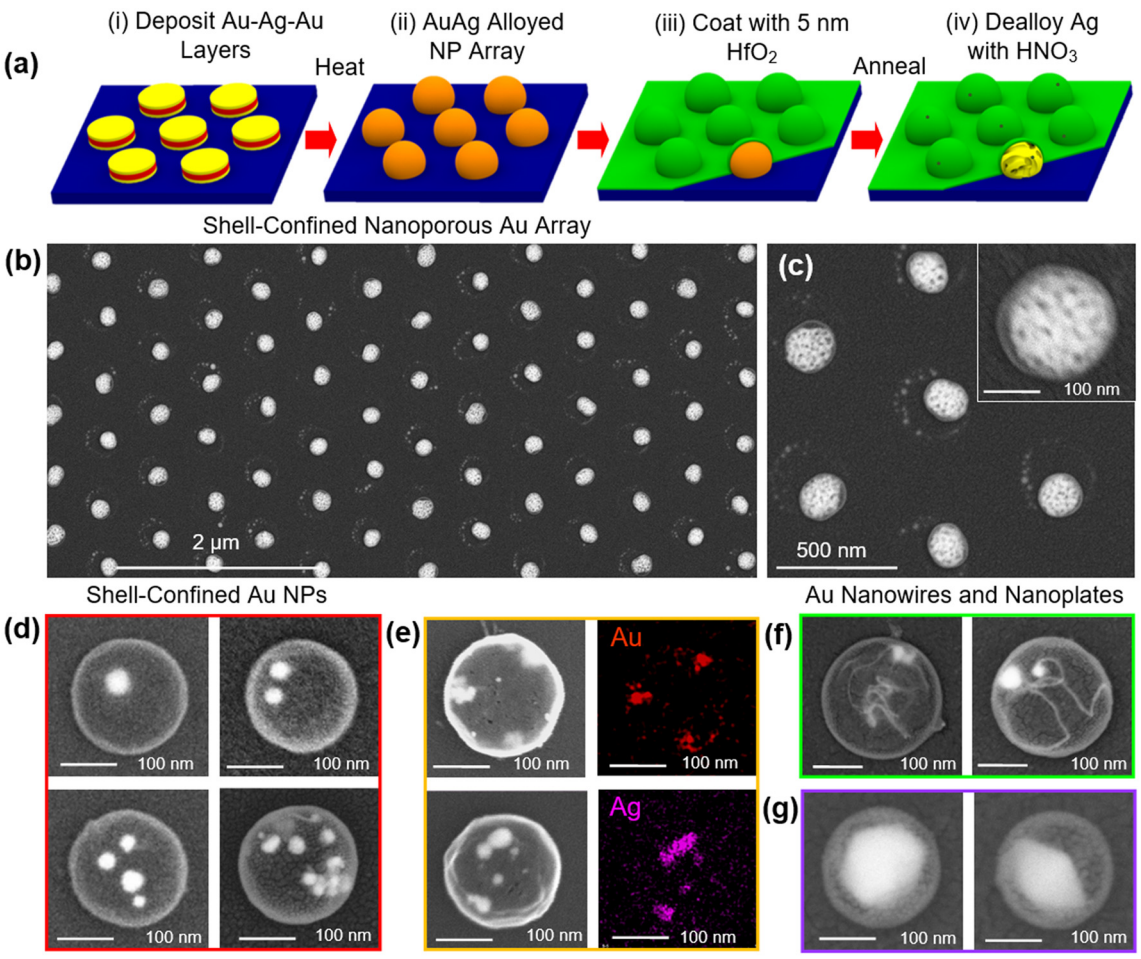

Fig. 3 (a) Schematic of the procedure used to form nanoporous Au within the confines of a HfO_2 nanoshell. (b) Low and (c) high magnification BSE SEM images of an array of nanoporous Au nanostructures. BSE SEM images demonstrating the confinement of (d) varying numbers of Au nanoparticles, (e) Au and Ag NPs and the associated elemental mapping, (f) Au nanowires, and (g) Au nanoplates.

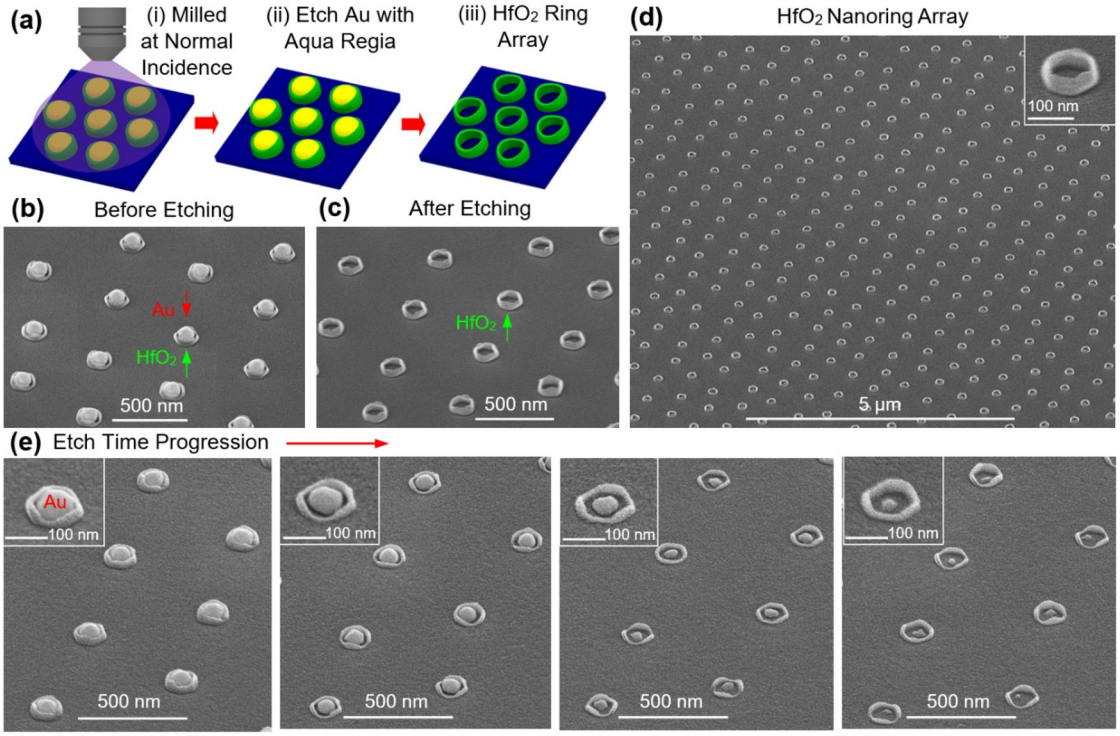

Fig. 4 (a) Schematic of the procedure used to form periodic arrays of HfO_2 nanorings. Tilted-view SEM images of (b) Au@HfO_2 core–shell structures after being exposed to a directional Ar^+ ion beam that selectively removes the oxide from the top of the Au structure and (c) the HfO_2 nanorings formed through the removal of the Au. (d) Large-area image of the nanoring array. (e) Time series of SEM images showing Au NPs diminishing in size as they are progressively etched.

nanomaterials derivable from this technique by disrupting the conformal nature of the ALD-deposited oxide. Fig. 4a shows a schematic illustrating this concept as it pertains to the formation of periodic arrays of HfO_2 nanorings. Arrays of near-hemispherical Au NPs, coated with a conformal HfO_2 layer, are first fabricated using the previously outlined procedure and then exposed to a collimated ion beam that is directed at the substrate surface at normal incidence. Under optimized milling conditions, the oxide layer encapsulating each Au structure is selectively milled from the top surface, exposing the underlying Au. The sacrificial Au structures are then etched away using *aqua regia*, leaving behind a HfO_2 ring at each of the array positions. The inner diameter of the ring is, hence, determined by the size of the initial Au structure while the ring width is set by the thickness of the HfO_2 deposited. It should also be noted that ion milling, because it partially exposes the Au surface, negates the need for the annealing procedure that creates nanopores. Fig. 4b and c show SEM images of the milled structures obtained before and after the etching step where it is apparent that the Au is first exposed and then removed. Fig. 4d shows a large-area image of the ring array that demonstrates that such structures can be produced in high yield, a result that further indicates that these thin rings are robust to the milling/etching processing steps. With etching proceeding from an exposed Au surface, as opposed to nanopore(s), the removal process becomes far more isotropic, allowing for the formation of plasmonic structures of variable sizes that are encircled by an oxide ring (Fig. 4e). Such configurations are not readily achievable through lithographic or self-assembly processes.

Once Ar^+ ion milling is incorporated into the overall nanofabrication strategy, it opens up additional possibilities. For example, the formation of near-hemispherical Au@HfO_2 core–shell structures followed by an ion milling process directed at normal incidence that removes just the top of the structures leads to formation of open-topped HfO_2 nanobowls once the Au is removed (see ESI, Fig. S6†). Carrying out the nanoring procedure shown in Fig. 4a, but where the near-hemispherical structures are substituted for faceted nanoplates, gives rise to hexagonal nanorings (see ESI, Fig. S7†). Altering the milling direction such that the oxide is selectively removed from different portions of the Au template adds another level of versatility. Fig. 5a shows a schematic of a fabrication process that is identical with that which forms nanorings (Fig. 4) but where the milling is carried out at a 9° glancing angle. Under these conditions, the oxide is milled away on one side of the structure but where the backside is protected by a self-shadowing effect. Removal of the remaining Au with *aqua regia* leaves behind an array of vertically standing half-shells. Fig. 5b show SEM images of the HfO_2-coated Au nanostructures after the milling process where the initially complete 10 nm thick oxide shell is removed from one side of the structure along with a

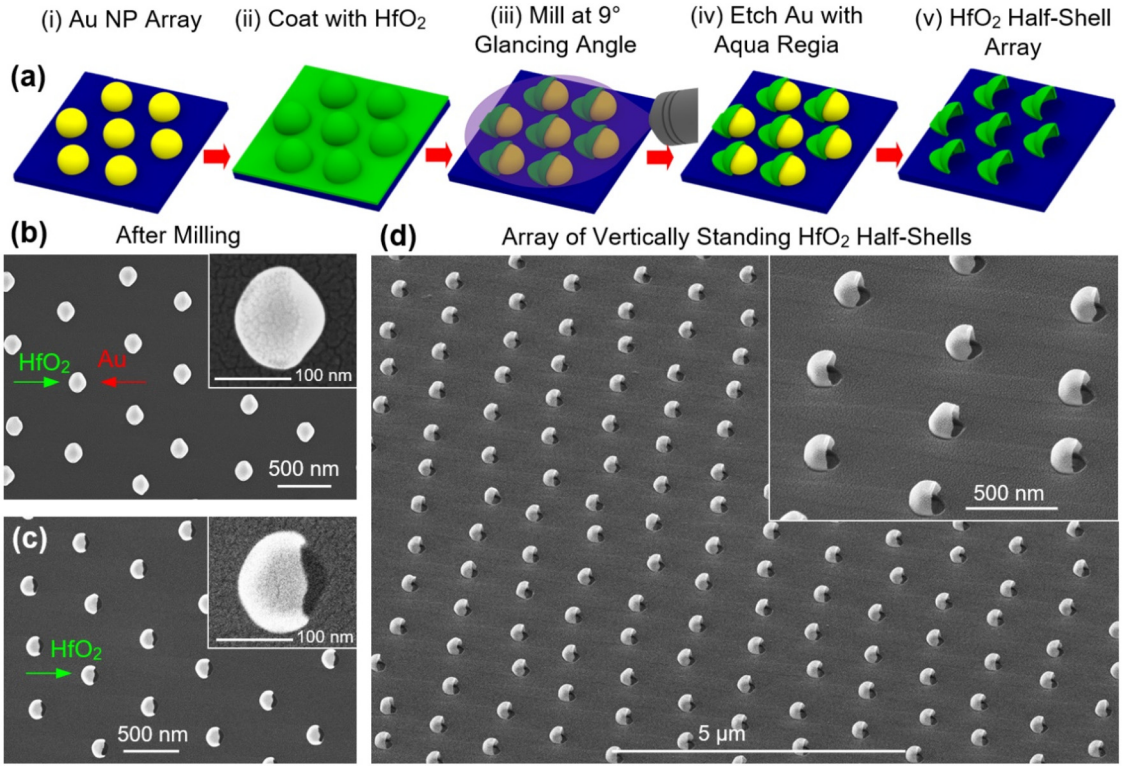

Fig. 5 (a) Schematic showing the procedure used to obtain periodic arrays of vertically standing half-shells of HfO_2 where each is identically aligned on the substrate surface. (b) Top-view SEM image of the Au@HfO_2 core–shell structures after being milled at a 9° glancing angle and (c) the same structures after Au removal. (d) Tilted-view SEM images of a periodic array of HfO_2 half-shells.

portion of the Au template. The final structures, obtained after the remainder of the Au template is removed, appear as an array of identically aligned vertical half-shells (Fig. 5c and d). Behind each of the structures are remnants of the HfO_2 layer that remain unscathed because they were protected from the ion beam by the shadow cast by individual structures. With other possibilities stemming from variations to the milling direction, template shape, and the choice of ALD-deposited materials, there exist numerous opportunities from which unique architectures can be obtained.

Discussion

The current study demonstrates the use of metal nanostructures as sacrificial templates in the fabrication of organized surfaces of substrate-bound oxide nanostructures with three-dimensional configurations. By combining lithographic techniques, directed-assembly, ALD, liquid-phase seed-mediated syntheses, and ion milling, the work not only brings together a collection of techniques that are not routinely practiced together but also demonstrates the effectiveness of such approaches in realizing structures that are unobtainable using standalone methods. It also highlights the effectiveness of nanofabrication schemes that take advantage of the chemically dissimilar properties exhibited by metals and oxides where, in the current study, the chemical stability of HfO_2 is exploited by having it remain intact when exposed to *aqua regia*, an etchant that is highly corrosive to metals. Beyond the initial demonstrations presented here, there exist numerous opportunities for preparing oxide surfaces with well-ordered topographies and individual nanostructures with sophisticated architectures. Even though the current study focused on the use of Au nanocrystal templates, this is, by no means, a requirement but was instead done to take advantage of existing capabilities. Templates can be produced from any ALD-compatible material where a preferential etch exists and can even take the form of lithographically patterned polycrystalline films or shape-engineered colloids dispersed onto a substrate. Likewise, HfO_2 can be substituted by a rather expansive set of materials available through the ALD technique that include other oxides, nitrides, sulfides, and selenides, each of which express their own unique properties.[1–5] As such, there exists a versatile design space from which functional nanomaterials can be derived.

Organized surfaces of ALD-generated oxide nanomaterials have potential for application in a number of areas. As demonstrated, hollow shells with nanopore openings represent configurations suitable for nanoreactor applications. Substrate-confined nanoreactors[56] represent a burgeoning field that is complemented by a well-established colloidal counterpart that sees nanoparticle synthesis carried out within the confines of porous shells and then utilized as vehicles in catalytic, bio-

medical, and energy-related applications.[58–60] With the ability to perform nanostructure syntheses within the inner volume of porous shells firmly established,[59,61–63] there also exists the intriguing possibility of forming structures within substrate-based nanoshells followed by a procedure that seals the openings to obtain liquid-filled capsules housing mobile nanostructures. With the resulting structures realizing a 'ship in a bottle' motif, such capsule-confined structures could prove ideal for active plasmonic applications[64–66] whereby an altered plasmonic response is obtained when the structures are subjected to an external stimulus. As open-topped nanobowls, the HfO_2 structures represent liquid-containment vessels suitable for carrying out reactions where precursors occupy attoliter volumes.[67,68] Vertically standing half-shells and shape-controlled rings could find utility as topographical features that serve as (i) trapping sites for colloidal structures in directed assembly processes,[48,69] (ii) obstacles to nanostructure growth fronts that define nanogaps between adjacent structures,[41] and (iii) supports onto which two-dimensional materials are overlayed to realize contours that locally alter electronic, photonic, and mechanical properties.[70–73] Taken together, these oxide structures have the potential to act as a unique platform for advancing the capabilities of substrate-based nanomaterials.

Conclusion

Nanofabrication routes have been forwarded for forming oxide nanoshells, open-topped bowls, vertically standing half-shells, and shape-controlled rings on substrates in periodic arrays. The procedures set forth capitalize on (i) the unique capabilities of the ALD technique, (ii) the chemically distinct behaviors of oxides and metals, (iii) a high-temperature annealing procedure that leads to the formation of nanopores in ALD-deposited shells, and (iv) a collimated ion beam that is able to selectively mill material from topographical surfaces. The work lays the foundation for a host of potential applications and contributes to a broad-based effort directed toward expanding the nanomaterial landscape through the implementation of new tools and strategies.

Experimental section

Chemicals and materials

Two-side polished [0001]-oriented sapphire substrates were sourced from MTI Corporation as 100 mm diameter wafers and diced into smaller pieces (10.5 mm × 10 mm × 0.65 mm). The nanoimprint lithography process used a (i) bilayer resist composed of mr-I 7030R (Micro Resist Technology, GmbH) and polydimethylglutarimide (PMGI SF 3S), (ii) tetramethylammonium hydroxide, 8, III developer (CD-26, Kayaku Advanced Materials) diluted to 40% with H_2O, and (iii) dioxolane solvent (EBR-PG, Kayaku Advanced Materials). Stamps for imprinting were obtained from Lightsmyth Technologies, after which a trichloro-(1*H*,2*H*,2*H*-perfluorooctyl)silane antisticking layer (MilliporeSigma) was applied. The Au used in the array making process was sputter deposited from a 19 mm diameter target that was punched from a 1.0 mm thick foil with 99.9985% purity (Alfa Aesar). Tetrakis-(ethylmethylamido) hafnium (TEMAH, MilliporeSigma) was used as the ALD precursor for the deposition of HfO_2. The *aqua regia* used to etch Au was a 1 : 1 mixture of 6 M hydrochloric acid (HCl, VWR) and 2 M nitric acid (HNO_3, Beantown Chemical). Reagents used when forming the Au templates shown in Fig. 2b–d are chloroauric acid ($HAuCl_4$, 99.99% trace metal basis, Beantown Chemical), silver nitrate ($AgNO_3$, reagent ACS, Ward's Science), trisodium citrate dihydrate ($Na_3C_6H_5O_7{\cdot}2H_2O$, 99% pure, Thermo Scientific), Brij-700 block copolymer (Average MW 4,670, Spectrum Chemicals), and 4-(2-hydroxyethyl)-1-piperazineethanesulfonic acid (HEPES buffer, 99%, VWR). Additional reagents used when carrying out the nanoreactor syntheses shown in Fig. 3 are ascorbic acid (AA, MilliporeSigma), aniline ($C_6H_5NH_2$, 99+%, Alfa Aesar), polyvinylpyrrolidone (40 000 MW PVP, MilliporeSigma), and methanol (VWR). Deionized (DI) water with a resistivity of 18.2 MΩ cm was used for the preparation of all aqueous solutions.

HfO_2 nanoshells

Periodic arrays of near-hemispherical Au NPs were fabricated using procedures described elsewhere.[49,74] Briefly, nanoimprint lithography was used to define hexagonal arrays of polycrystalline Au disks on [0001]-oriented sapphire substrates. Samples were then subjected to a heating regimen under flowing Ar that causes each disk to assemble into a near-hemispherical [111]-oriented single-crystal structure where a heteroepitaxial relationship is formed between Au and the underlying substrate.[75] A 5 nm thick conformal HfO_2 layer was then deposited at 200 °C over the Au structures using ALD. The deposition cycle, which was repeated 50 times, consisted of alternating 200 ms TDMAH and 20 ms H_2O vapor exposures carried out at a nominal flow rate of 20 sccm where each was followed by a N_2 gas purge lasting 10 s and 8 s, respectively. The role of the purge is to inhibit precursor intermixing and flush away reaction byproducts. The so-formed oxide layers are amorphous and have an ill-defined stoichiometry. Nanopores were formed in the HfO_2 shells by annealing the arrayed Au@HfO_2 core–shell structures using a heating sequence that sees them heated in an Ar gas flow to 770 °C over the course of 14 min, held at this temperature for 30 min, and then gradually cooled to room temperature over a 2 h period. Au removal proceeded using a 60 min *aqua regia* etch (Hazard: *aqua regia* is highly toxic and corrosive). The sample is then transferred to DI H_2O where it remains for 1 min after which it placed in acetone for 1 min before drying. The role of the acetone is to displace the H_2O so that the structures dry in a liquid that exerts a reduced capillary force on the fragile nanoshells.[76] HfO_2 nanoshells produced with nanocube, nanoplate, and nanostar morphologies were fabricated using the same procedure except that the initial templates were produced using

liquid-state seed-mediated syntheses that are described in detail elsewhere.[53–55]

HfO_2 nanorings, nanobowls, and vertical half-shells

Periodic arrays of HfO_2-coated Au NPs were fabricated using the aforementioned procedures but where no anneal step occurred. Nanoring formation then proceeded by exposing the array to a collimated Ar^+ ion beam for 10 s. The beam, which was directed at the substrate at normal incidence, was generated using a 0.7 keV excitation energy, a current of 8.0 μA, and a gas flow of 0.1 sccm. With HfO_2 removed from the uppermost portions of the Au template, the structures were exposed to an *aqua regia* etch for 60 min, leaving behind an array of nanorings. Nanobowls were produced in much the same manner except that the HfO_2 thickness was increased to 20 nm to give the nanobowl sidewalls additional mechanical strength and the Ar^+ ion milling conditions were optimized for this process (t = 60 s, E = 0.5 keV, I = 6.7 μA, flow = 0.1 sccm). The vertically standing half-shells were also similarly made except that the ion beam was directed at a 9° glancing angle for 20 s (E = 3 keV, I = 14.7 μA, flow = 0.1 sccm) and the thickness of the HfO_2 layer was set to 10 nm.

Nanoreactor syntheses

The preparation of nanoporous Au (Fig. 3b and c) began by defining periodic arrays of Au–Ag–Au trilayer disks with layer thicknesses of 4.5, 18, and 4.5 nm. The disks were then assembled into near-hemispherical alloyed structures by heating them to 700 °C in 12 min followed by a 15 min dwell at 700 °C in flowing Ar. A HfO_2 layer containing nanopores was then formed over the structures using the aforementioned procedures. The Ag component was dealloyed from the structures through their exposure to HNO_3 (5 mL, 15.8 M) for 60 min. Shell-confined Au and Ag nanoparticles (Fig. 3d and e) were formed in a synthesis that sees empty HfO_2 shells immersed in AA (5 ml, 10 mM) for 2 h, after which they were removed from the solution and immediately submerged in $HAuCl_4$ or $AgNO_3$ (2 mL, 10 mM) for 1 h. Repeating this sequence, without letting the samples dry, led to an increased number of nanoparticles within the shell. Au nanowire synthesis (Fig. 3f) proceeded through a 20 min exposure of shell-confined Au nanoparticles to a 10 mL aqueous growth solution containing aniline (0.5 mL, 50 mM), $HAuCl_4$ (0.5 ml, 10 mM), PVP (0.6 mL, 0.5 mM), and methanol (2 mL). Au nanoplate synthesis (Fig. 3g) saw shell-confined Au nanoparticles exposed to a 10 mL aqueous solution containing $HAuCl_4$ (0.5 ml, 10 mM), PVP (0.6 mL, 0.5 mM), and methanol (2 mL) for 2 h under LED lighting.[77] It should be noted that the nanoplate synthesis yielded few structures with the desired morphology. For all nanoreactor syntheses, no specific measures were taken to prevent nucleation and growth outside of the shell. Any colloidal structures that are produced are rinsed away at the end of the synthesis.

Instrumentation

Au nanocrystal array fabrication utilized a (i) home-built imprinter, (ii) Laurell WS-650-23 B spin coater, (iii) Samco RIE-1C reactive ion etching system, (iv) model 681 Gatan high resolution ion beam coater, and (v) Lindberg Blue M furnace fitted with a quartz tube and an Ar gas handling system. HfO_2 depositions were carried out in a Savannah 100 ALD system. Ion milling took place in a Gatan model 685 PECS II system. SEM images were taken with a FEI Helios G4 UX DualBeam SEM/FIB workstation. A JASCO V-730 UV–Visible Spectrophotometer was used for spectroscopic characterization.

Conflicts of interest

There are no conflicts to declare.

Acknowledgements

This work was supported by the National Science Foundation, Division of Chemistry, Macromolecular, Supramolecular, and Nanochemistry (MSN) Program under Grant No. CHE-2107728 to S. N. It has also benefited from the facilities available through the Notre Dame Integrated Imaging Facility (NDIIF). W. J. T. acknowledges support received through a Notre Dame Materials Science and Engineering Fellowship.

References

1 S. Yasmeen, S. Ryu, S.-H. Lee and H.-B.-R. Lee, Atomic Layer Deposition Beyond Thin Film Deposition Technology, *Adv. Mater. Technol.*, 2022, **9**, 2200876.
2 T. J. Kunene, L. K. Tartibu, K. Ukoba and T.-C. Jen, Review of Atomic Layer Deposition Process, Application and Modeling Tools, *Mater. Today: Proc.*, 2022, **62**, S95–S109.
3 R. W. Johnson, A. Hultqvist and S. F. Bent, A Brief Review of Atomic Layer Deposition: From Fundamentals to Applications, *Mater. Today*, 2014, **17**, 236–246.
4 J. Ponraj, G. Attolini and M. Bosi, Review on Atomic Layer Deposition and Applications of Oxide Thin Films, *Crit. Rev. Solid State Mater. Sci.*, 2013, **38**, 203–233.
5 S. M. George, Atomic Layer Deposition: An Overview, *Chem. Rev.*, 2010, **110**, 111–131.
6 X. Zeng, Y. Zhao, X. Hu, G. D. Stucky and M. Moskovits, Rational Component and Structure Design of Noble-Metal Composites for Optical and Catalytic Applications, *Small Struct.*, 2021, **2**, 2000138.
7 S. Vempati, K. S. Ranjith, F. Topuz, N. Biyikli and T. Uyar, Electrospinning Combined with Atomic Layer Deposition to Generate Applied Nanomaterials: A Review, *ACS Appl. Nano Mater.*, 2020, **3**, 6186–6209.
8 Z. Zhang, Y. Zhao, Z. Zhao, G. Huang and Y. Mei, Atomic Layer Deposition-Derived Nanomaterials: Oxides,

Transition Metal Dichalcogenides, and Metal–Organic Frameworks, *Chem. Mater.*, 2020, **32**, 9056–9077.

9 J. Prakash, H. C. Swart, G. Zhang and S. Sun, Emerging Applications of Atomic Layer Deposition for the Rational Design of Novel Nanostructures for Surface-Enhanced Raman Scattering, *J. Mater. Chem. C*, 2019, **7**, 1447–1471.

10 N. Biyikli and A. Haider, Atomic Layer Deposition: An Enabling Technology for the Growth of Functional Nanoscale Semiconductors, *Semicond. Sci. Technol.*, 2017, **32**, 093002.

11 B. J. O'Neill, D. H. K. Jackson, J. Lee, C. Canlas, P. C. Stair, C. L. Marshall, J. W. Elam, T. F. Kuech, J. A. Dumesic and G. W. Huber, Catalyst Design with Atomic Layer Deposition, *ACS Catal.*, 2015, **5**, 1804–1825.

12 A. S. Preston, R. A. Hughes, T. B. Demille and S. Neretina, Plasmonics under Attack: Protecting Copper Nanostructures from Harsh Environments, *Chem. Mater.*, 2020, **32**, 6788–6799.

13 L. Ma, Y. Huang, M. Hou, Z. Xie and Z. Zhang, Ag Nanorods Coated with Ultrathin TiO2 Shells as Stable and Recyclable SERS Substrates, *Sci. Rep.*, 2015, **5**, 15442.

14 Y. Zhang, J.-H. Bahk, J. Lee, C. S. Birkel, M. L. Snedaker, D. Liu, H. Zeng, M. Moskovits, A. Shakouri and G. D. Stucky, Hot Carrier Filtering in Solution Processed Heterostructures: A Paradigm for Improving Thermoelectric Efficiency, *Adv. Mater.*, 2014, **26**, 2755–2761.

15 S. Standridge, G. Schatz and J. Hupp, Toward Plasmonic Solar Cells: Protection of Silver Nanoparticles via Atomic Layer Deposition of TiO_2, *Langmuir*, 2009, **25**, 2596–2600.

16 A. S. Preston, R. A. Hughes, N. L. Dominique, J. P. Camden and S. Neretina, Stabilization of Plasmonic Silver Nanostructures with Ultrathin Oxide Coatings Formed Using Atomic Layer Deposition, *J. Phys. Chem. C*, 2021, **125**, 17212–17220.

17 B. J. O'Neill, D. H. K. Jackson, A. J. Crisci, C. A. Farberow, F. Shi, A. C. Alba-Rubio, J. Lu, P. J. Dietrich, X. Gu, C. L. Marshall, P. C. Stair, J. W. Elam, J. T. Miller, F. H. Ribeiro, P. M. Voyles, J. Greeley, M. Mavrikakis, S. L. Scott, T. F. Kuech and J. A. Dumesic, Stabilization of Copper Catalysts for Liquid-Phase Reactions by Atomic Layer Deposition, *Angew. Chem., Int. Ed.*, 2013, **52**, 13808–13812.

18 J. Lee, D. H. K. Jackson, T. Li, R. E. Winans, J. A. Dumesic, T. F. Kuech and G. W. Huber, Enhanced Stability of Cobalt Catalysts by Atomic Layer Deposition for Aqueous-Phase Reactions, *Energy Environ. Sci.*, 2014, **7**, 1657.

19 J. S. Daubert, G. T. Hill, H. N. Gotsch, A. P. Gremaud, J. S. Ovental, P. S. Williams, C. J. Oldham and G. N. Parsons, Corrosion Protection of Copper Using Al_2O_3, TiO_2, ZnO, HfO_2, and ZrO_2 Atomic Layer Deposition, *ACS Appl. Mater. Interfaces*, 2017, **9**, 4192–4201.

20 M. Wang, X. Cheng, T. Cao, J. Niu, R. Wu, X. Liu and Y. Zhang, Constructing Ultrathin TiO2 Protection Layers Via Atomic Layer Deposition for Stable Lithium Metal Anode Cycling, *J. Alloys Compd.*, 2021, **865**, 158748.

21 C. Li and Y. Jin, Shell-Isolated Plasmonic Nanostructures for Biosensing, Catalysis, and Advanced Nanoelectronics, *Adv. Funct. Mater.*, 2021, **31**, 2008031.

22 J. Krajczewski and A. Kudelski, Shell-Isolated Nanoparticle-Enhanced Raman Spectroscopy, *Front. Chem.*, 2019, **7**, 410.

23 C. Soldano, M. A. Ashworth, G. D. Wilcox, T. Kutilainen, J. Hokka, J. Praks and M. Pudas, Atomic Layer Deposition (ALD) for Environmental Protection and Whisker Mitigation of Electronic Assemblies, *CEAS Space J.*, 2023, **15**, 113–126.

24 F. A. A. Nugroho, D. Albinsson, T. J. Antosiewicz and C. Langhammer, Plasmonic Metasurface for Spatially Resolved Optical Sensing in Three Dimensions, *ACS Nano*, 2020, **14**, 2345–2353.

25 G. Albrecht, M. Ubl, S. Kaiser, H. Giessen and M. Hentschel, Comprehensive Study of Plasmonic Materials in the Visible and Near-Infrared: Linear, Refractory, and Nonlinear Optical Properties, *ACS Photonics*, 2018, **5**, 1058–1067.

26 J. Seo, S. Jeon, S. Lee, D.-K. Lim, J. H. Kim, J. H. Kim, S. Ahn and W. Jung, Oxidative Strong Metal-Support Interaction Induced by an Amorphous TiO_x Seed Layer Boosts the Electrochemical Performance and High-Durability of Pt Nanocatalysts, *ACS Catal.*, 2022, **12**, 8593–8600.

27 Y. Yuan, Z. Huang, S. Hu, D. Cai and G. Zhan, Pt-Based Nanoreactors Derived from ZIF-67 Nanocubes on Al_2O_3 Films for Low-Temperature CO Oxidation, *ACS Appl. Nano Mater.*, 2022, **5**, 9882–9892.

28 H. Feng, J. Lu, P. C. Stair and J. W. Elam, Alumina Over-Coating on Pd Nanoparticle Catalyst by Atomic Layer Deposition: Enhanced Stability and Reactivity, *Catal. Lett.*, 2011, **141**, 512–517.

29 T. M. Onn, S. Zhang, L. Arroyo-Ramirez, Y.-C. Chung, G. W. Graham, X. Pan and R. J. Gorte, Improved Thermal Stability and Methane-Oxidation Activity of Pd/Al_2O_3 Catalysts by Atomic Layer Deposition, *ACS Catal.*, 2015, **5**, 5696–5701.

30 M. Higashino, S. Murai and K. Tanaka, Improving the Plasmonic Response of Silver Nanoparticle Arrays via Atomic Layer Deposition Coating and Annealing above the Melting Point, *J. Phys. Chem. C*, 2020, **124**, 27687–27693.

31 G. Albrecht, S. Kaiser, H. Giessen and M. Hentschel, Refractory Plasmonics without Refractory Materials, *Nano Lett.*, 2017, **17**, 6402–6408.

32 S. Huo, Y. Wu, C. Zhao, F. Yu, J. Fang and Y. Yang, Core–Shell $TiO_2@Au_{25}/TiO_2$ Nanowire Arrays Photoanode for Efficient Photoelectrochemical Full Water Splitting, *Ind. Eng. Chem. Res.*, 2020, **59**, 14224–14233.

33 S. Mubeen, J. Lee, W. R. Lee, N. Singh, G. D. Stucky and M. Moskovits, On the Plasmonic Photovoltaic, *ACS Nano*, 2014, **8**, 6066–6073.

34 S. D. Standridge, G. C. Schatz and J. T. Hupp, Distance Dependence of Plasmon-Enhanced Photocurrent in Dye-Sensitized Solar Cells, *J. Am. Chem. Soc.*, 2009, **131**, 8407–8409.

35 H. Peeters, M. Keulemans, G. Nuyts, F. Vanmeert, C. Li, M. Minjauw, C. Detavernier, S. Bals, S. Lenaerts and S. W. Verbruggen, Plasmonic Gold-Embedded TiO_2 Thin Films as Photocatalytic Self-Cleaning Coatings, *Appl. Catal., B*, 2020, **267**, 118654.

36 L. M. Vogl, P. Schweizer, L. Pethö, A. Sharma, J. Michler and I. Utke, From Metal Nanowires to Ultrathin Crystalline ALD Nanotubes: Process Development and Mechanism Revealed by In Situ TEM Heating Experiments, *Nanoscale*, 2023, **15**, 9477–9483.

37 J. Zhang, W. Yu, D. Feng, H. Xu and Y. Qin, Porous Titania Nanotube Confined Ultrafine Platinum Catalysts Synthesized by Atomic Layer Deposition with Enhanced Hydraulic Dehydration Performance, *Appl. Catal., B*, 2022, **312**, 121405.

38 N. Yan, Q. Guan, Z. Yang, M. Feng, X. Jiang, J. Liu and L. Xu, Synthesis of Double-Shelled Hollow Inorganic Nanospheres through Block Coploymer-Metal Coordination and Atomic Layer Deposition, *Polymers*, 2019, **11**, 1208.

39 R. H. A. Ras, M. Kemell, J. de Wit, M. Ritala, G. ten Brinke, M. Leskela and O. Ikkala, Hollow Inorganic Nanospheres and Nanotubes with Tunable Wall Thicknesses by Atomic Layer Deposition on Self-Assembled Polymeric Templates, *Adv. Mater.*, 2007, **19**, 102–106.

40 J. T. Korhonen, P. Hiekkataipale, J. Malm, M. Karppinen, O. Ikkala and R. H. A. Ras, Inorganic Hollow Nanotube Aerogels by Atomic Layer Deposition onto Native Nanocellulose Templates, *ACS Nano*, 2011, **5**, 1967–1974.

41 Z. L. Lawson, A. S. Preston, M. T. Korsa, N. L. Dominique, W. J. Tuff, E. Sutter, J. P. Camden, J. Adam, R. A. Hughes and S. Neretina, Plasmonic Gold Trimers and Dimers with Air-Filled Nanogaps, *ACS Appl. Mater. Interfaces*, 2022, **14**, 28186–28198.

42 Y. Q. Cao, K. Qin, L. Zhu, X. Qian, X. J. Zhang, D. Wu and A. D. Li, Atomic-Layer-Deposition Assisted Formation of Wafer-Scale Double-Layer Metal Nanoparticles with Tunable Nanogap for Surface-Enhanced Raman Scattering, *Sci. Rep.*, 2017, **7**, 5161.

43 H. Im, K. C. Bantz, S. H. Lee, T. W. Johnson, C. L. Haynes and S. H. Oh, Self-Assembled Plasmonic Nanoring Cavity Arrays for SERS and LSPR Biosensing, *Adv. Mater.*, 2013, **25**, 2678–2685.

44 H. Im, K. C. Bantz, N. C. Lindquist, C. L. Haynes and S.-H. Oh, Vertically Oriented Sub-10 nm Plasmonic Nanogap Arrays, *Nano Lett.*, 2010, **10**, 2231–2236.

45 W. J. Tuff, R. A. Hughes, S. D. Golze and S. Neretina, Ion Beam Milling as a Symmetry-Breaking Control in the Synthesis of Periodic Arrays of Identically Aligned Bimetallic Janus Nanocrystals, *ACS Nano*, 2023, **17**, 4050–4061.

46 G. A. Vinnacombe-Willson, Y. Conti, A. Stefancu, P. S. Weiss, E. Cortés and L. Scarabelli, Direct Bottom-Up In Situ Growth: A Paradigm Shift for Studies in Wet-Chemical Synthesis of Gold Nanoparticles, *Chem. Rev.*, 2023, **123**, 8488–8529.

47 H. Zhang, C. Kinnear and P. Mulvaney, Fabrication of Single-Nanocrystal Arrays, *Adv. Mater.*, 2020, **32**, 1904551.

48 R. A. Hughes, E. Menumerov and S. Neretina, When Lithography Meets Self-Assembly: A Review of Recent Advances in the Directed Assembly of Complex Metal Nanostructures on Planar and Textured Surfaces, *Nanotechnology*, 2017, **28**, 282002.

49 E. Menumerov, S. D. Golze, R. A. Hughes and S. Neretina, Arrays of Highly Complex Noble Metal Nanostructures using Nanoimprint Lithography in Combination with Liquid-Phase Epitaxy, *Nanoscale*, 2018, **10**, 18186–18194.

50 T. Li, S. Karwal, B. Aoun, H. Zhao, Y. Ren, C. P. Canlas, J. W. Elam and R. E. Winans, Exploring Pore Formation of Atomic Layer-Deposited Overlayers by in Situ Small- and Wide-Angle X-ray Scattering, *Chem. Mater.*, 2016, **28**, 7082–7087.

51 S. Karwal, T. Li, A. Yanguas-Gil, C. P. Canlas, Y. Lei, A. U. Mane, J. A. Libera, S. Seifert, R. E. Winans and J. W. Elama, Tailoring Nanopore Formation in Atomic Layer Deposited Ultrathin Films, *J. Vac. Sci. Technol., A*, 2018, **36**, 01A103.

52 F. Mazzotta, T. Johnson, A. Dahlin, J. Shaver, S. Oh and F. Höök, Influence of the Evanescent Field Decay Length on the Sensitivity of Plasmonic Nanodisks and Nanoholes, *ACS Photonics*, 2015, **2**, 256–262.

53 M. Hajfathalian, K. D. Gilroy, R. A. Hughes and S. Neretina, Citrate-Induced Nanocubes: A Reexamination of the Role of Citrate as a Shape-Directing Capping Agent for Ag-Based Nanostructures, *Small*, 2016, **12**, 3444–3452.

54 T. B. Demille, R. D. Neal, A. S. Preston, Z. Liang, A. G. Oliver, R. A. Hughes and S. Neretina, Epitaxially Aligned Single-Crystal Gold Nanoplates Formed in Large-Area Arrays at High Yield, *Nano Res.*, 2021, **15**, 296–303.

55 T. B. Demille, R. A. Hughes, N. Dominique, J. E. Olson, S. Rouvimov, J. P. Camden and S. Neretina, Large-Area Periodic Arrays of Gold Nanostars Derived from HEPES-, DMF-, and Ascorbic-Acid-Driven Syntheses, *Nanoscale*, 2020, **12**, 16489–16500.

56 J. H. Swisher, L. Jibril, S. H. Petrosko and C. A. Mirkin, Nanoreactors for Particle Synthesis, *Nat. Rev.*, 2022, **7**, 428–448.

57 D. Wang and P. Schaaf, Nanoporous Gold Nanoparticles, *J. Mater. Chem.*, 2012, **22**, 5344–5348.

58 C. Gao, F. Lyu and Y. Yin, Encapsulated Metal Nanoparticles for Catalysis, *Chem. Rev.*, 2021, **121**, 834–881.

59 L.-S. Lin, J. Song, H.-H. Yang and X. Chen, Yolk–Shell Nanostructures: Design, Synthesis, and Biomedical Applications, *Adv. Mater.*, 2018, **30**, 1704639.

60 L. Yu, H. Hu, H. B. Wu and X. W. Lou, Complex Hollow Nanostructures: Synthesis and Energy-Related Applications, *Adv. Mater.*, 2017, **29**, 1604563.

61 A. Li, W. Zhu, C. Li, T. Wang and J. Gong, Rational Design of Yolk–Shell Nanostructures for Photocatalysis, *Chem. Soc. Rev.*, 2019, **48**, 1874–1907.

62 R. Purbia and S. Paria, Yolk/Shell Nanoparticles: Classifications, Synthesis, Properties, and Applications, *Nanoscale*, 2015, **7**, 19789–19873.
63 L. Guodong and Z. Tang, Noble Metal Nanoparticle@Metal Oxide Core/Yolk-Shell Nanostructures as Catalysts: Recent Progress and Perspective, *Nanoscale*, 2014, **6**, 3995–4011.
64 N. Jiang, X. Zhuo and J. Wang, Active Plasmonics: Principles, Structures, and Applications, *Chem. Rev.*, 2018, **118**, 3054–3099.
65 Z. Li and Y. Yin, Stimuli-Responsive Optical Nanomaterials, *Adv. Mater.*, 2019, **31**, 1807061.
66 S. Homaeigohar and M. Elbahri, Switchable Plasmonic Nanocomposites, *Adv. Opt. Mater.*, 2019, **7**, 1801101.
67 J. E. Barton and T. W. Odom, Mass-Limited Growth in Zeptoliter Beakers: A General Approach for the Synthesis of Nanocrystals, *Nano Lett.*, 2004, **4**, 1525–1528.
68 L. Wang, M. H. Lee, J. Barton, L. Hughes and T. W. Odom, Shape-Control of Protein Crystals in Patterned Microwells, *J. Am. Chem. Soc.*, 2008, **130**, 2142–2143.
69 S. Ni, L. Isa and H. Wolf, Capillary Assembly as a Tool for the Heterogeneous Integration of Micro- and Nanoscale Objects, *Soft Matter*, 2018, **14**, 2978–2995.
70 J. M. Kim, C. Cho, E. Y. Hsieh and S. W. Nam, Heterogeneous Deformation of Two-Dimensional Materials for Emerging Functionalities, *J. Mater. Res.*, 2020, **35**, 1369–1385.
71 J. Kern, I. Niehues, P. Tonndorf, R. Schmidt, D. Wigger, R. Schneider, T. Stiehm, S. M. de Vasconcellos, D. E. Reiter, T. Kuhn and R. Bratschitsch, Nanoscale Positioning of Single-Photon Emitters in Atomically Thin WSe_2, *Adv. Mater.*, 2016, **28**, 7101–7105.
72 S. M. Rehn, T. M. Gerrard-Anderson, L. Qiao, Q. Zhu, G. Wehmeyer and M. R. Jones, Mechanical Reshaping of Inorganic Nanostructures with Weak Nanoscale Forces, *Nano Lett.*, 2021, **21**, 130–135.
73 S. M. Rehn, T. M. Gerrard-Anderson, Y. Chen, P. Wang, S. Robertson, T. P. Senftle and M. R. Jones, Surface Ligands Dictate the Mechanical Properties of Inorganic Nanomaterials, *ACS Nano*, 2023, **17**, 6698–6707.
74 R. D. Neal, Z. R. Lawson, W. J. Tuff, K. Xu, V. Kumar, M. T. Korsa, M. Zhukovskyi, M. R. Rosenberger, J. Adam, J. P. Camden, R. A. Hughes and S. Neretina, Large-Area Periodic Arrays of Atomically Flat Single-Crystal Gold Nanotriangles formed Directly on Substrate Surfaces, *Small*, 2022, **18**, 2205780.
75 S. D. Golze, R. A. Hughes, E. Menumerov, S. Rouvimov and S. Neretina, Synergistic Roles of Vapor- and Liquid-Phase Epitaxy in the Seed-Mediated Synthesis of Substrate-Based Noble Metal Nanostructures, *Nanoscale*, 2021, **13**, 20225–20233.
76 A. S. Preston, R. A. Hughes, T. B. Demille and S. Neretina, Copper Template Design for the Synthesis of Bimetallic Copper-Rhodium Nanoshells through Galvanic Replacement, *Part. Part. Syst. Charact.*, 2018, **35**, 1700420.
77 S. D. Golze, R. A. Hughes, S. Rouvimov, R. D. Neal, T. B. Demille and S. Neretina, Plasmon-Mediated Synthesis of Periodic Arrays of Gold Nanoplates using Substrate-Immobilized Seeds Lined with Planar Defects, *Nano Lett.*, 2019, **19**, 5653–5660.